RSC Advances

PAPER

View Article Online
View Journal | View Issue

Check for updates

Cite this: *RSC Adv.*, 2025, **15**, 28348

ZnO electrocatalyst integrated onto carbon paper for efficient non-aqueous Li–O_2 batteries

Inhan Kang, Sehun Kim, Su Min Lee, Se Hyun Jeong, Hyeong Ju Ki, Ui Jin Lee, Jae Hyung Ko, Byung Jun Son, Sungjin Kim* and Jungwon Kang *

Received 20th May 2025
Accepted 25th July 2025

DOI: 10.1039/d5ra03545g

rsc.li/rsc-advances

The development of high-performance lithium–oxygen (Li–O_2) batteries is hindered by challenges including high overpotential and limited cycle life. In this paper, we report the cost-effective and scalable synthesis of a ZnO electrocatalyst directly integrated onto carbon paper *via* a simple dipping and thermal treatment method. The resulting ZnO-on-carbon composite (ZnO on P50) was employed as the cathode in a non-aqueous Li–O_2 battery. Comprehensive physicochemical characterizations, including XPS, FE-SEM, and TEM, confirmed the successful incorporation and uniform dispersion of ZnO nanoparticles within the carbon matrix. Electrochemical evaluations revealed that the ZnO-based cathode reduced overpotential during charge–discharge cycles and improved energy efficiency by approximately 6.3% over 40 cycles compared to pristine carbon paper (P50). *Ex situ* XRD and SEM analyses further validated the formation and decomposition of Li_2O_2 during cycling and suggested enhanced reaction uniformity owing to the catalytic role of ZnO. These findings demonstrate that *in situ*-grown ZnO offers a promising, low-cost strategy for improving the energy efficiency of Li–O_2 batteries.

Open Access Article. Published on 11 August 2025. Downloaded on 6/15/2026 7:57:33 AM.
This article is licensed under a Creative Commons Attribution 3.0 Unported Licence.

Introduction

Lithium–oxygen (Li–O_2) batteries have garnered considerable attention owing to their exceptionally high theoretical energy density, surpassing that of conventional energy storage systems.[1,2] Among the four types (aprotic, aqueous, all-solid-state, and hybrid aqueous/aprotic) of Li–O_2 batteries,[3] rechargeable aprotic Li–O_2 batteries typically consist of a lithium metal anode, non-aqueous Li^+-conducting electrolyte, and a porous cathode. In a typical discharge reaction, oxygen undergoes reduction and reacts with lithium ions to form lithium peroxide (Li_2O_2), which primarily accumulates on the surface of the air electrode, and the reverse process occurs during charging: $2Li^+ + O_2 + 2e^- \leftrightarrow Li_2O_2$ ($E^0 = 2.96$ V, *vs.* Li/Li^+).[4,5] Despite these promising features, several important technical challenges, including electrolyte degradation, safety issues related to lithium metal anodes, and high overpotentials (*i.e.*, the voltage gap between charge and discharge), must be addressed to enable the commercialization of Li–O_2 batteries. One of the main obstacles in developing non-aqueous Li–O_2 batteries is the large polarization during discharge, and especially during charge (>1.0 V), due to the formation and decomposition of the insulating discharge product, Li_2O_2. This high polarization results in low energy efficiency and poor cycling stability.[6,7]

To address these limitations, considerable efforts have focused on incorporating electrocatalysts, such as metals and metal oxides, into carbon-based materials.[8] However, the use of certain catalysts poses challenges, such as the reliance on expensive precious metals (*e.g.*, Pt, Ru, Au, and Ir)[9–12] and the complex synthesis routes required for some metal oxides (*e.g.*, $CuCo_2O_4$ and $NiCo_2O_4$).[13,14] Several studies have investigated ZnO-based catalysts for non-aqueous Li–O_2 batteries. Luo *et al.* reported that Pd nanoparticles uniformly dispersed on ZnO-passivated porous carbon, synthesized *via* atomic layer deposition, functioned effectively as a cathode material, showing high catalytic activity, particularly for the oxygen evolution reaction.[15] Yin *et al.* developed hierarchical mesoporous ZnO/$ZnFe_2O_4$/C nanocages, derived from MOF templates, which exhibited a high discharge capacity (>11 000 mAh g^{-1} at 300 mA g^{-1}) and improved cyclability performance (5000 mAh g^{-1} over 15 cycles) when used as a Li–O_2 battery cathode.[16] However, these approaches often require costly noble metals or involve complex synthetic procedures. Dai *et al.* synthesized $CoMn_2O_4$ using a solvothermal reaction and a polystyrene template and achieved 286 cycles at a current density of 200 mA g^{-1}. This was deposited in the form of a film of Li_2O_2 due to the enhanced adsorption capacity of the LiO_2 intermediate, and the DFT results proved that oxygen vacancies are advantageous for LiO_2 adsorption.[17] Lin *et al.* achieved 272 cycles at 200 mA g^{-1} by forming low-crystalline Co-oxide and atomic-level dispersion of Ru (double-solvent method) through MOF-based synthesis using ZIF precursor. They reported that low-crystalline cobalt oxide has adsorption properties that promote the formation of

Department of Advanced Materials Science and Engineering, Mokpo National University, 61 Dorim-ri, 1666 Yeongsan-ro, Cheonggye-myeon, Muan-gun, 58554, Jeonnam, South Korea. E-mail: ksj840711@gmail.com; jwkang17@mokpo.ac.kr

© 2025 The Author(s). Published by the Royal Society of Chemistry

Open Access Article. Published on 11 August 2025. Downloaded on 6/15/2026 7:57:33 AM. This article is licensed under a Creative Commons Attribution 3.0 Unported Licence.

film-like LiO_2 intermediate, and when ruthenium is dispersed at the atomic level, the ORR/OER catalytic activity and Li_2O_2 decomposition efficiency are significantly increased.[18]

In this study, we demonstrated the direct *in situ* incorporation of ZnO on carbon paper using a simple dipping and thermal treatment method and evaluated its application in non-aqueous Li–O_2 batteries. The resulting rechargeable Li–O_2 cell, employing a ZnO electrocatalyst-integrated carbon paper cathode, exhibited an average ~6.3% reduction in charge–discharge overpotential over 40 cycles.

Experimental

Preparation of materials

Zinc acetate dihydrate ($Zn(CH_3COO)_2 \cdot 2H_2O$, Daejung) was dissolved in ethylene glycol (Daejung). Carbon paper (P50, AvCarb®) was immersed in the solution in an amount of 0.01 mol and heated at 400 °C in air for 10 h. After heating, the ZnO electrocatalyst-integrated carbon paper was punched to 12 mm and dried overnight at 120 °C in a vacuum oven.

The moisture in *N,N*-dimethylacetamide (DMAc, Sigma-Aldrich), used as the electrolyte, was removed using activated molecular sieves with a pore size of 4 Å. Lithium nitrate ($LiNO_3$, Sigma-Aldrich) was also dried overnight at 120 °C in a vacuum oven. $LiNO_3$ was added to DMAc in an amount of 1 mol.

Characterization of materials

X-ray diffraction (XRD) patterns were recorded using an EMPYREAN/PANalytical multipurpose X-ray diffractometer. X-ray photoelectron spectroscopy (XPS) was carried out using an Al-Kα X-ray source (Multilab 2000, Thermo VG Scientific). The morphology and elemental distribution were examined by field-emission scanning electron microscopy (FE-SEM; S-4800, Hitachi) at 15 kV and field-emission transmission electron microscopy (FE-TEM; Tecnai F20, Philips) at 200 kV.

Fabrication of Li–O_2 cells

Swagelok-type cells were assembled in a glove box (MBraun; H_2O < 0.1 ppm, O_2 < 1 ppm). Each cell composed a lithium metal anode (Honjo Metal Co), a separator GF (Whatmann™), a carbon cathode (P50, AvCarb®), an electrolyte (DMAc-$LiNO_3$), a mesh current collector, and an O-ring. The mass loading of the active material was 6.5 mg, and 0.65 μg of electrolyte was used in each cell.

After assembly, high-purity oxygen gas (>99.995%) was introduced into the inlet and outlet tubes of the cells. An oxygen environment of approximately 1.5 bar was maintained during the charge–discharge cycling by keeping both inlet and outlet valves open. The electrochemical properties of the assembled Li–O_2 cells were analyzed using a VMP3 potentiostat.

Results and discussion

A ZnO electrocatalyst integrated onto carbon paper (ZnO on P50) was fabricated using a simple dipping and heating process, as described in the experimental section. Various electrocatalysts for Li–O_2 batteries have been developed in our laboratory using this method, including Mn_3O_4,[19] NiO,[20] CuO,[21]

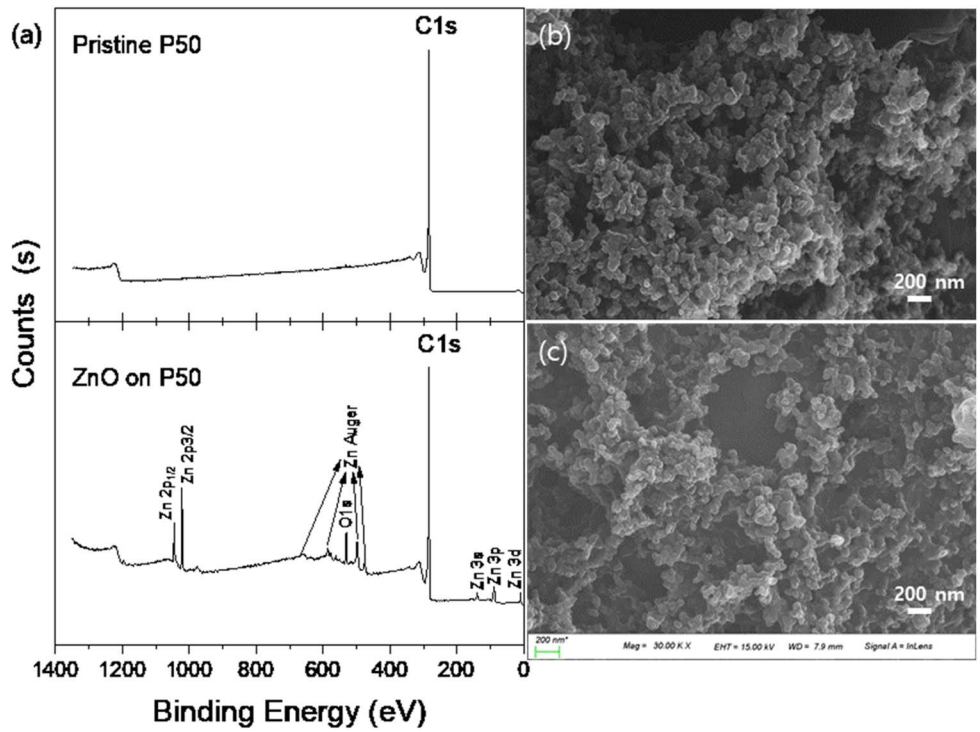

Fig. 1 XPS survey scan (a). FE-SEM images of the pristine P50 (b) and ZnO on P50 (c).

Open Access Article. Published on 11 August 2025. Downloaded on 6/15/2026 7:57:33 AM.
This article is licensed under a Creative Commons Attribution 3.0 Unported Licence.

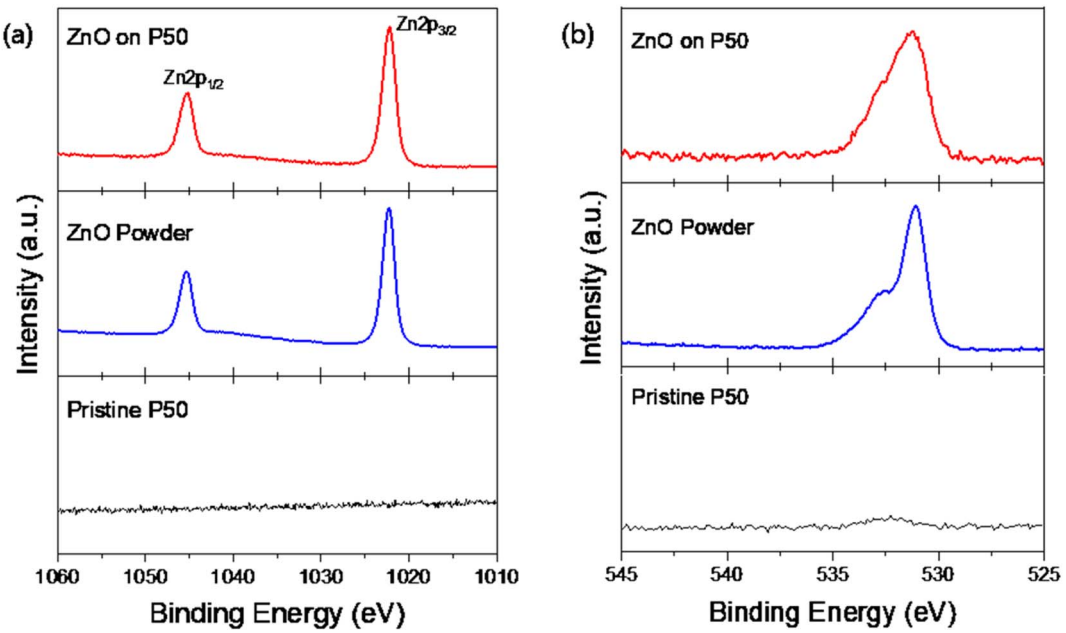

Fig. 2 High resolution XPS spectra in the core-level region of Zn 2p (a) and O 1s (b).

Fe_2O_3,[22] and $CaCO_3$.[23] In most cases, XRD peaks were not clearly observed, likely because of the extremely small amounts of catalyst produced during synthesis. Similarly, the ZnO on P50 in this study did not exhibit any distinguishable ZnO peaks in the XRD patterns when compared with pristine P50, as shown in Fig. S1. Fig. S2 presents the XRD patterns of ZnO and ZnO powder prepared by heating zinc acetate monohydrate at 400 °C in air. This is consistent with the results in the paper by other reports.[24–26] This observation is consistent with previous findings on electrocatalysts from our laboratory: the ZnO content in the ZnO electrocatalyst-integrated carbon was insufficient for detection by XRD. Therefore, more sensitive surface analysis techniques, such as XPS, are necessary to confirm the presence of ZnO.

Fig. 1 shows the XPS survey scan (a) and FE-SEM images of pristine P50 (b) and ZnO on P50 (c). When comparing pristine P50 (Fig. 1b) and ZnO on P50 (Fig. 1c), no significant morphological differences are observed. In the XPS survey scans (Fig. 1a), of pristine P50 and ZnO on P50 for binding energy range of 0–1400 eV, only a C 1s peak at ~284 eV appears in pristine P50, while distinct Zn, O, and C peaks were detected in ZnO on P50. No trace contaminants resulting from the simple dipping and heating process are observed on the surface of ZnO on P50 sample.[27] The elemental analysis from XPS suggests that the actual loading amount of ZnO is approximately 18 wt%.

Fig. 2 shows the high-resolution XPS *spectra* of Zn 2p (Fig. 2a) and O 1s (Fig. 2b). In the range 1010–1060 eV, the Zn 2p core-level XPS spectra of ZnO on P50 (red) and ZnO powder (blue) displayed doublet splitting at approximately 1022 and 1045 eV, corresponding to Zn $2p_{1/2}$ and Zn $2p_{3/2}$ core-levels, respectively.[28] However, no distinguishable peaks were detected for the pristine P50 (black, Fig. 2a). Similarly, the O 1s spectra for both ZnO on P50 and ZnO powder show peaks at approximately 532 eV, while the pristine P50 exhibited no corresponding peak (Fig. 2b).[29] These results indicate that the presence of ZnO, which was not detectable in the XRD analysis of ZnO on P50 (Fig. S1), was successfully identified through the XPS survey spectrum, and a minor quantity of ZnO was integrated within the carbon network of ZnO on P50. Fig. 3 shows the curve-fitted O 1s spectra of ZnO on P50 and ZnO powders, which further

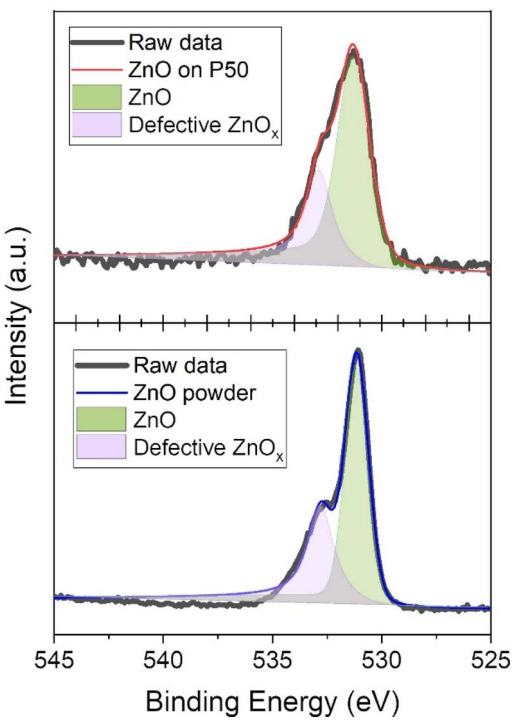

Fig. 3 Curve-fitted O 1s spectra of ZnO on P50 and ZnO powder.

© 2025 The Author(s). Published by the Royal Society of Chemistry

Open Access Article. Published on 11 August 2025. Downloaded on 6/15/2026 7:57:33 AM.
This article is licensed under a Creative Commons Attribution 3.0 Unported Licence.

demonstrates the difference in chemical composition between the two samples. The two asymmetric peaks are associated with the O_2^- ions within the typical wurtzite ZnO lattice (light green) and the O_2^- ions within the oxygen-deficient region (defective ZnO_x, light purple) in both ZnO on P50 and ZnO powder. Oxygen vacancies, as one of the most prevalent point defects in metal oxides, have been extensively recognized for their crucial role in enhancing the electrochemical performance of lithium–air batteries. These vacancies introduce localized electronic states near the conduction band, often leading to significant modifications of the electronic structure. Specifically, oxygen-deficient sites generate defect states within the band gap, effectively narrowing the band gap and increasing the density of free carriers. As a result, the electrical conductivity of the metal oxide is markedly improved, which facilitates faster charge transfer kinetics during both the oxygen reduction reaction (ORR) and oxygen evolution reaction (OER) processes.[30] In addition to electronic enhancements, oxygen vacancies function as catalytically active sites that strengthen the adsorption and activation of oxygen species. The under-coordinated metal centers formed adjacent to vacancy sites provide electron-rich environments that promote strong interaction with molecular oxygen (O_2) and superoxide intermediates (O_2^-). This strengthened adsorption not only lowers the activation barrier for O_2 reduction but also enables the stabilization of reactive ORR intermediates, such as LiO_2. The stabilization of LiO_2 plays a key role in directing the reaction pathway toward the formation of $Li_{2-x}O_2$—a non-stoichiometric, electronically conductive discharge product that offers lower overpotential and enhanced reversibility compared to stoichiometric Li_2O_2.[31,32]

The notable differences in chemical composition between the two samples became even clearer upon examination of the curve-fitted O 1s spectra of ZnO on P50 and ZnO powder, as illustrated in Fig. 3. The two asymmetric peaks are associated with the O_2^- ions in the typical wurtzite ZnO lattice (light green) and O_2^- ions located in oxygen-deficient regions within the ZnO matrix (defective ZnO_x, light purple) in both ZnO on P50 and ZnO powder samples.[33,34]

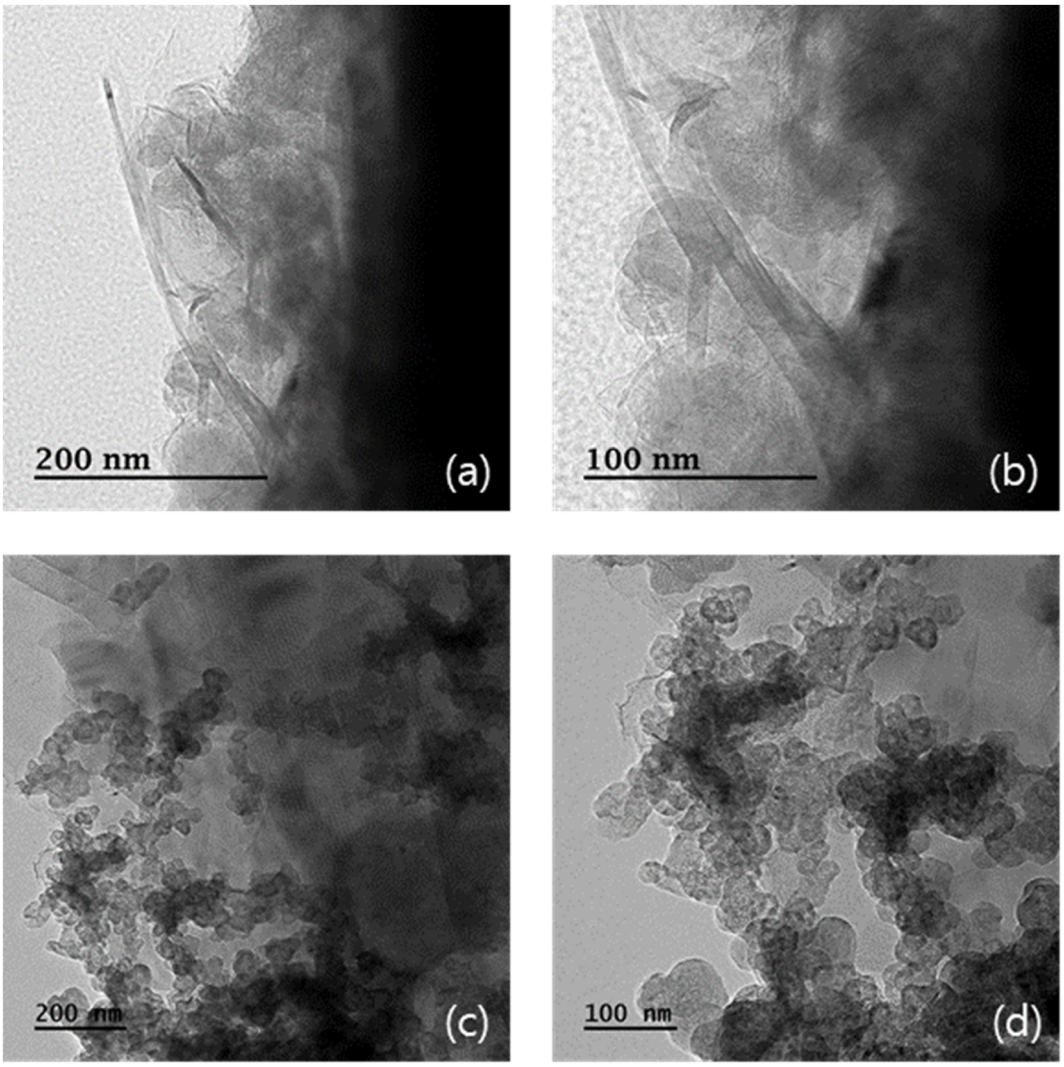

Fig. 4 FE-TEM images of the pristine P50 (a and b) and ZnO on P50 (c and d).

Open Access Article. Published on 11 August 2025. Downloaded on 6/15/2026 7:57:33 AM.
This article is licensed under a Creative Commons Attribution 3.0 Unported Licence.

The morphologies and particle structures of the prepared samples were verified using HR-TEM. Fig. 4 presents the HR-TEM images of pristine P50 (a and b) and ZnO on P50 (c and d). Amorphous features are exclusively observed in pristine P50 (Fig. 4a and b), indicating the presence of carbon without distinct particulate structures. By contrast, spherical particles are clearly visible and well dispersed within the amorphous carbon matrix in ZnO on P50, as shown in Fig. 4c and d.

Elemental mapping analysis clearly shows the features of ZnO on P50, in which the ZnO particles are uniformly distributed within the carbon matrix. Fig. 5 shows the dark-field (a) and elemental mapping (b) images, and the corresponding elements for C (c), O (d), and Zn (e) of ZnO on P50. The dark-field TEM image of ZnO on P50 (Fig. 5a) reveals the presence of spherical nanoparticles, which is further corroborated by EDS elemental mapping (Fig. 5b). The mapping in Fig. 5b shows that Zn (red) and O (pastel blue) are uniformly distributed across the C (green) background, and their respective elemental maps are displayed in Fig. 5c–e. This provides additional evidence that ZnO was successfully integrated into the carbon matrix.

Fig. 6 presents the lattice fringe images and SAED (Selected Area Electron Diffraction) patterns of the P50 and ZnO on P50 composites. Fig. 6a shows a high-resolution TEM image of P50, revealing a characteristic amorphous structure along with embedded carbon nanofibers. In the ZnO on P50 sample, ZnO crystallites are clearly observed, and the magnified inset (Fig. 6c, highlighted by the white box) displays distinct lattice fringes within the ZnO nanocrystals, along with observable structural defects attributed to oxygen vacancies. The measured d-spacing of the fringe is approximately 0.148 nm, corresponding to the (103) plane of wurtzite ZnO. The SAED pattern of ZnO on P50 in Fig. 6d shows a noticeably different diffraction pattern compared to pristine P50, with well-defined rings corresponding to $d(103) = 0.148$ nm, $d(102) = 0.191$ nm, and $d(201) = 0.136$ nm. These values are consistent with the (102), (103), and (201) planes of wurtzite ZnO. The presence of clear lattice fringe and diffraction rings confirms the nanocrystalline nature of ZnO containing oxygen vacancies, thereby verifying the crystallinity of the ZnO on P50 composite.

The ZnO on P50 composite was subsequently employed as the cathode material in a rechargeable non-aqueous Li–O_2

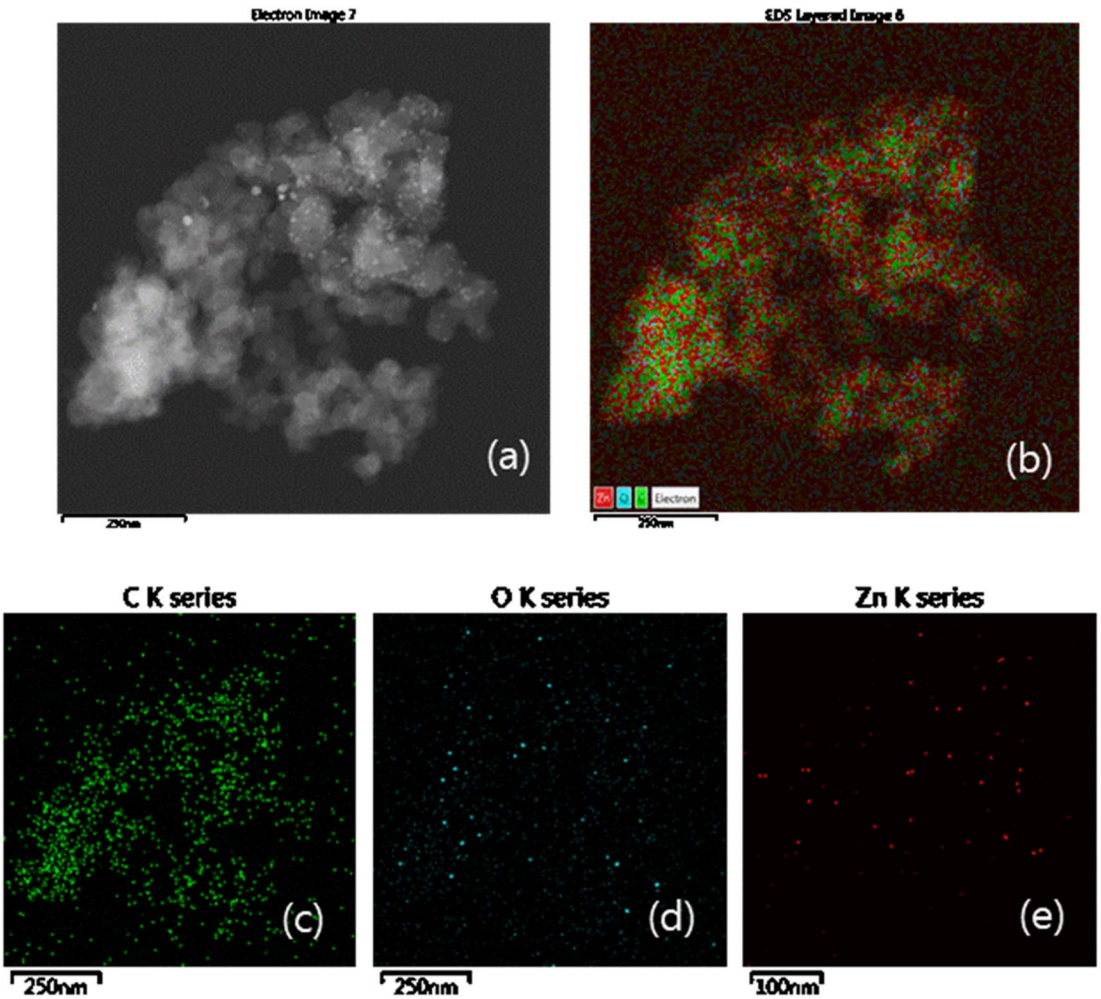

Fig. 5 Dark field TEM image (a). EDS elemental mapping images (b) and the corresponding elemental maps for C (c), O (d) and Zn (e) of ZnO on P50.

© 2025 The Author(s). Published by the Royal Society of Chemistry

Open Access Article. Published on 11 August 2025. Downloaded on 6/15/2026 7:57:33 AM.
This article is licensed under a Creative Commons Attribution 3.0 Unported Licence.

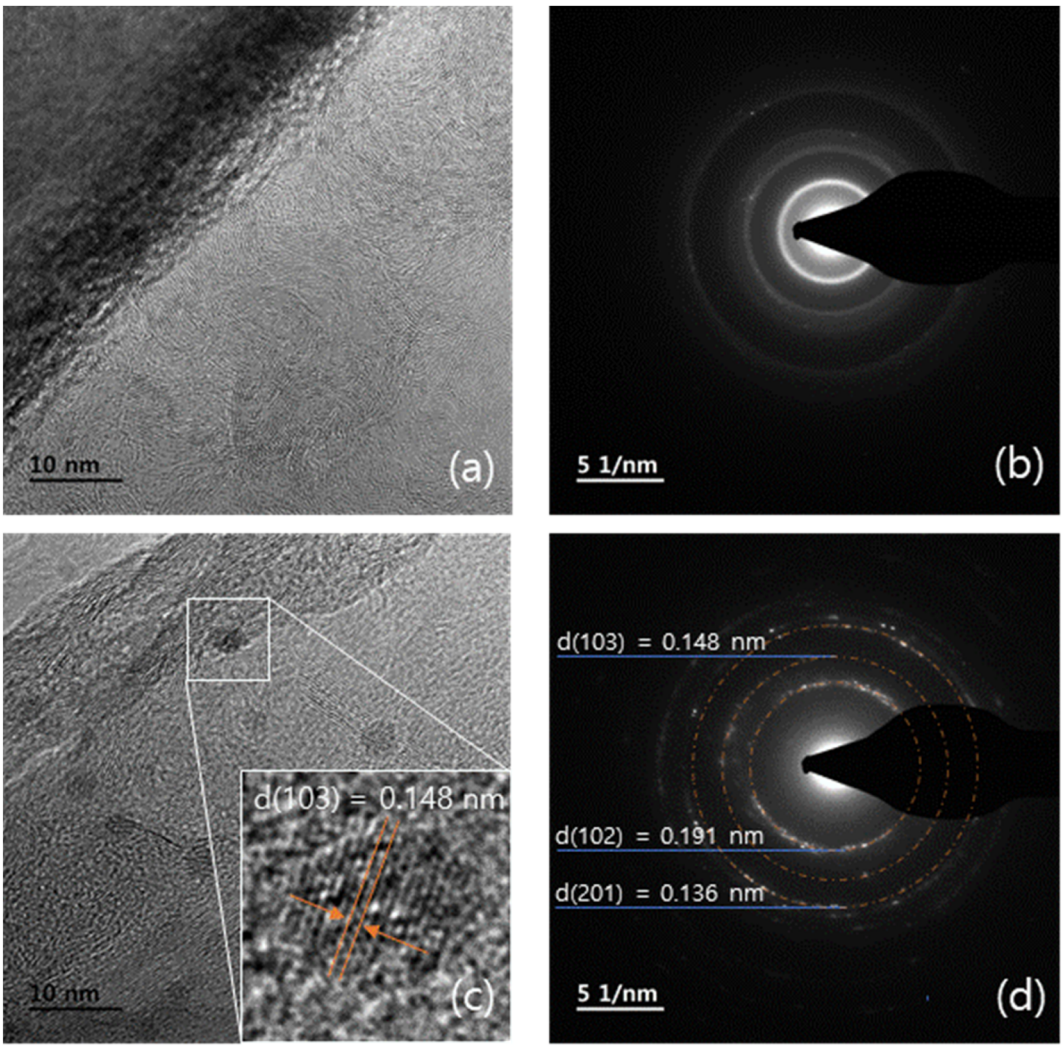

Fig. 6 Lattice fringe of P50 (a), ZnO On P50 (c) and SAED analysis of P50 and ZnO on P50 (b and d).

battery. Fig. 6 shows the 1st (a), 10th (b), 20th (c), 30th (d), and 40th (e) discharge–charge profiles at a current of 0.1 mA for 5 h (limiting capacity: 0.5 mAh). Results are shown for both pristine P50 (black) and ZnO on P50 (red). The cycling performance and corresponding energy efficiencies are summarized in Fig. 6f. In the initial few cycles, there was little noticeable improvement; however, after the fifth cycle, an increase of approximately 6% was observed in energy efficiency, with stable operation maintained up to 40 cycles, as depicted in Fig. 6e.

Fig. S3 shows that the ZnO on P50 sample exhibits improved cycling stability, reaching 75 cycles compared to 50 cycles for the pristine P50. Although the cycle life of the ZnO on P50 sample is limited to fewer than 100 cycles in this study, the result primarily reflects the catalytic effect of ZnO, rather than a fully optimized system. Therefore, achieving a cycle life beyond 100 cycles with ZnO on P50 is considered feasible through further optimization in future studies.

In lithium–air battery systems, the decline in coulombic efficiency is closely related with parasitic reactions and incomplete OER (oxygen evolution reactions) that occur on the cathode surface during the charging process. These detrimental effects lead to the accumulation of residual by-products, which reduce the active surface area available in subsequent cycles. As a result, coulombic efficiency progressively decreases, accompanied by poor cycle-to-cycle reproducibility and shortened cycle life. During the initial cycles, both samples exhibit comparable coulombic efficiencies, as negligible parasitic reactions and incomplete OER occur, leaving minimal residuals. However, a significant divergence emerges after the fifth cycle. This behavior is attributed to the formation of highly conductive and low-volume discharge products generated *via* the bifunctional cathode mechanism, which effectively mitigates the accumulation of resistive by-products and preserves the electrochemical activity of the cathode surface.[35]

We tabulate the performance and synthetic complexity of other metal oxides, including ZnO, and show that ZnO exhibits superior cycle properties compared to other oxides, as well as low cost and facile synthesis method. Although our previous studies applied easy synthetic methods, catalysts such as RuO_2

© 2025 The Author(s). Published by the Royal Society of Chemistry

Open Access Article. Published on 11 August 2025. Downloaded on 6/15/2026 7:57:33 AM. This article is licensed under a Creative Commons Attribution 3.0 Unported Licence.

Table 1 Properties of various metal oxides

Catalysts	Performance	Cost	Synthesis complexity
ZnO	40 cycles	Low	Simple (dipping & heating)
Mn_3O_4	40 cycles	Low	Simple (dipping & heating)
NiO	50 cycles	Medium	Simple (dipping & heating)
CuO	9 cycles	Low	Simple (dipping & heating)
RuO_2	20 cycles	High	Complex (one-pot solvothermal reaction)
IrO_2	10 cycles	High	Complex (CVD & hydrothermal method)

(ref. 36) and IrO_2 (ref. 37) are expensive and require complex synthetic methods.

The catalytic effects of the ZnO on P50 catalyst on reducing overpotential and enhancing energy efficiency are understood with previous studies on bifunctional cathodes. According to the reported work by Fan *et al.* on ZnO@VACNT, O_2 undergoes oxygen reduction reactions (ORR) on the surface of carbon nanotubes (CNTs), forming superoxide (O_2^-), which is then either adsorbed at the ZnO/VACNT interface or dissolved into the electrolyte.[35] This reduced superoxide, possessing an abnormal oxidation state, facilitates the formation of non-stoichiometric, defect-rich $Li_{2-x}O_2$ discharge products, often referred to as LiO_2-like species (Table 1).

Compared to conventional Li_2O_2 products, $Li_{2-x}O_2$ exhibits lower overpotential during electrochemical reactions, along with higher electronic conductivity and reduced volume, resulting in significantly improved energy efficiency and energy density.[38] Although ZnO does not serve as a direct catalyst for redox reactions, it plays a crucial role in promoting the formation of LiO_2-like discharge products and stabilizing them by guiding the formation of nanostructured and uniformly distributed phases.

Ex situ XRD analysis was performed to confirm if the aprotic Li–O_2 battery operates as per theoretical principles. Fig. 7 presents the *ex situ* XRD patterns for each corresponding state of the cell using pristine P50 (a) and ZnO on P50 (b), where the formation of Li_2O_2 (red asterisk) during the discharge state and its disappearance upon the fully recharged state can be observed in both samples, excluding the expected undesirable byproducts. The LiOH (green inverted triangle) observed in the recharged state of the pristine P50 sample is believed to have formed during the XRD measurement process after washing, while the Li_2CO_3 (blue circle) detected in the discharged state of the ZnO on P50 possibly resulting from electrolyte decomposition induced by the catalyst. The O_2^- (superoxide) species generated on the surface or interface of defective ZnO contribute to the stabilization of LiO_2 intermediates, thereby enhancing the electrochemical performance of lithium–air batteries. However, the same reactive oxygen species participate in side reactions at the carbon electrode–electrolyte interface, leading to the formation of undesirable byproducts such as Li_2CO_3.[39] Li_2CO_3 is a highly irreversible byproduct that is difficult to decompose even at charging potentials above 4.38 V. Its continuous accumulation on the electrode surface leads to a significant reduction in active surface area, ultimately resulting in decreased coulombic efficiency and shortened cycle life. To address these challenges, several strategies have been proposed: (1) introducing redox-active species as charge

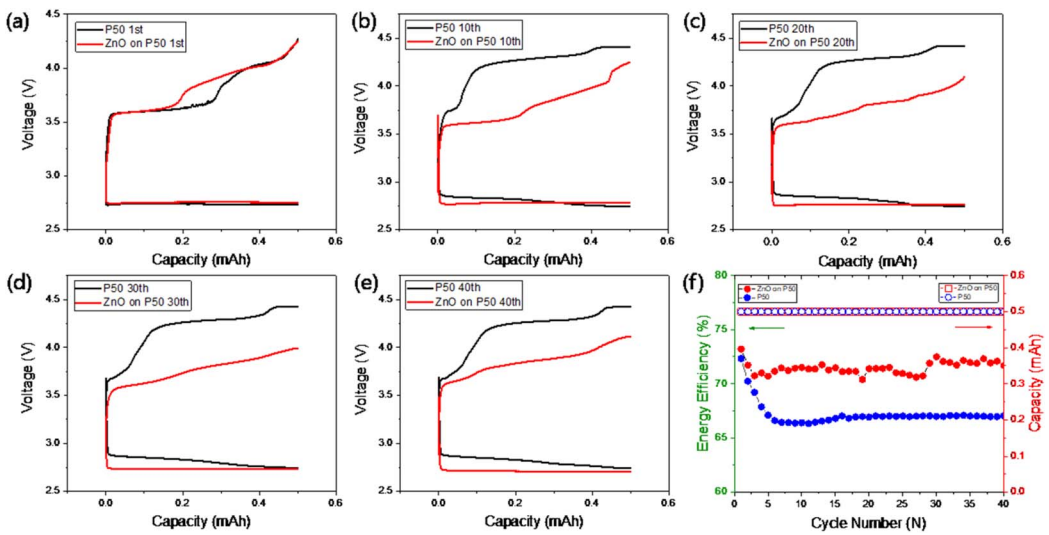

Fig. 7 1st (a), 10th (b), 20th (c), 30th (d) and 40th (e) discharge–charge profiles of the Li–O_2 cell using pristine P50 (black) and ZnO on P50 (red) at a current density of 0.5 mAh and their cycle performance and energy efficiency (f).

© 2025 The Author(s). Published by the Royal Society of Chemistry

Open Access Article. Published on 11 August 2025. Downloaded on 6/15/2026 7:57:33 AM.
This article is licensed under a Creative Commons Attribution 3.0 Unported Licence.

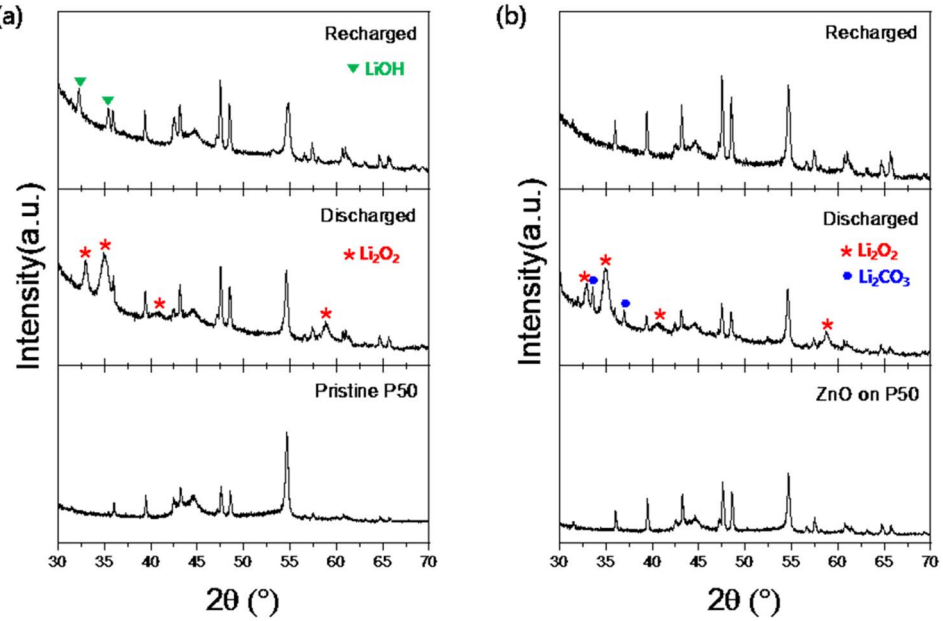

Fig. 8 *Ex situ* XRD patterns at different state of the Li–O_2 cell using pristine P50 (a) and ZnO on P50 (b).

mediators to compensate for electronic losses during charging, and (2) employing oxygen-selective membranes on the cathode to prevent the permeation of CO_2 and H_2O, thereby suppressing the formation of Li_2CO_3.[31,32] These approaches, if necessary, will be discussed in more detail in future studies.[40]

Fig. 8 shows SEM images of the discharge products (Li_2O_2). In the case of pristine P50 (Fig. 8a), agglomerated Li_2O_2 particles were observed. By contrast, the ZnO on P50 sample (Fig. 8b) exhibited a more uniform and finely distributed morphology. The uniformity of Li_2O_2 in ZnO on P50 is attributed to the well-defined active sites provided by ZnO, which were introduced into the carbon through an *in situ* direct growth method, thereby exhibiting a catalytic effect on the electrochemical properties of the aprotic Li–O_2 cell. The hierarchical mesoporous structure is composed of porous structures inside and outside the nanocage, providing diffusion channels for Li^+/O_2. In addition, ZZFC has a rational structure that combines the characteristics of large surface area and uniformly distributed active sites, which is advantageous for mass/electron transfer in multiphase discharge/charge reactions. It was reported that the TEGDME-based electrolyte is stable with ZZFC during operation, and the parasitic reaction is reduced, resulting in reversible generation/decomposition of Li_2O_2 as a discharge product.[16]

An ultra-low charge potential of 2.8 V was achieved by ALD-assisted ZnO passivation and Pd nanoparticle deposition, which is reported to be because the ALD ZnO thin films partially cover the carbon surface and selectively coat the carbon defect sites, which helps to minimize side reactions such as electrolyte decomposition and lithium carbonate formation at the defect sites. Previous density functional theory (DFT) calculations have shown that the small Al_2O_3 islands fabricated by ALD are small enough to be conductive by themselves, and in this case, a material more conductive than Al_2O_3, such as ZnO, is reported to be helpful for increasing the overall conductivity of the carbon anode when used to passivate the carbon defect sites (Fig. 9).[15]

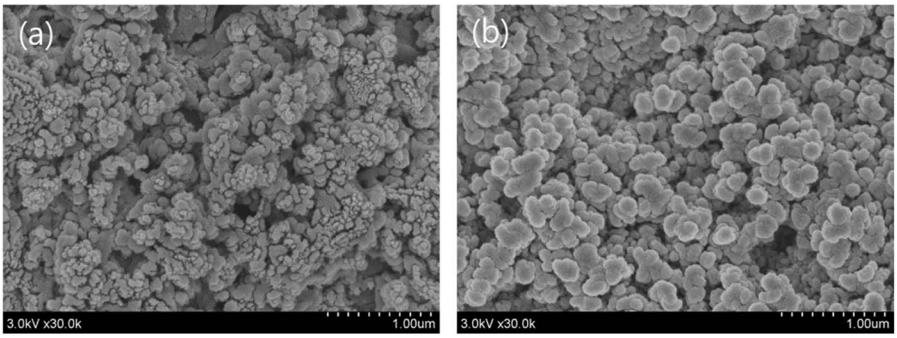

Fig. 9 SEM images of discharge product (Li_2O_2): pristine P50 (a), ZnO on P50 (b).

Open Access Article. Published on 11 August 2025. Downloaded on 6/15/2026 7:57:33 AM. This article is licensed under a Creative Commons Attribution 3.0 Unported Licence.

Conclusion

A ZnO electrocatalyst integrated onto carbon paper (ZnO on P50) was synthesized by a simple dipping of P50 carbon paper in a zinc acetate/ethylene glycol solution followed by heat treatment at 400 °C. The resulting ZnO on P50 was utilized as a cathode material for non-aqueous rechargeable Li–O_2 batteries. The Li–O_2 cell incorporating the ZnO on P50 cathode demonstrated an increase in energy efficiency of approximately 6.3% over 40 charge–discharge cycles.

Conflicts of interest

The authors declare no competing interests.

Data availability

The data used to support the findings of this study are included within the article.

The supplementary Information contain the results of XRD(ZnO on P50, P50, ZnO powder) and cycle ability(ZnO on P50, P50). See DOI: **https://doi.org/10.1039/d5ra03545g**.

Acknowledgements

This research was supported by the Basic Science Research Program through the National Research Foundation of Korea (NRF), funded by the Ministry of Education (2021R1I1A3057918).

References

1 L. Ma, T. Yu, E. Tzoganakis, K. Amine, T. Wu, Z. Chen and J. Lu, Fundamental understanding and material challenges in rechargeable nonaqueous Li–O_2 batteries: Recent progress and perspective, *Adv. Energy Mater.*, 2018, **8**, 1800348.

2 D. Wang, X. Mu, P. He and H. Zhou, Materials for advanced Li−O_2 batteries: Explorations, challenges and prospects, *Mater. Today*, 2019, **26**, 87–99.

3 J. Lu, L. Li, J. B. Park, Y. K. Sun, F. Wu and K. Amine, Aprotic and aqueous Li−O_2 batteries, *Chem. Rev.*, 2014, **114**, 5611–5640.

4 R. Cao, E. D. Walter, W. Xu, E. N. Nasybulin, P. Bhattacharya, M. E. Bowden, M. H. Engelhard and J.-G. Zhang, The mechanisms of oxygen reduction and evolution reactions in nonaqueous lithium–oxygen batteries, *ChemSusChem*, 2014, **7**, 2436–2440.

5 Y. Qiao, Y. Liu, K. Jiang, X. Li, Y. He, Q. Li, S. Wu and H. Zhou, Boosting the cycle life of aprotic Li–O_2 batteries *via* a photo-assisted hybrid Li_2O_2-scavenging strategy, *Small Methods*, 2012, **2**, 1700284.

6 C. Laoire, S. Mukerjee, E. J. Plichta, M. A. Hendrickson and K. M. Abraham, Rechargeable lithium/TEGDME-$LiPF_6$/O_2 battery, *J. Electrochem. Soc.*, 2011, **158**, A302–A308.

7 M. M. O. Thotiyl, S. A. Freunberger, Z. Peng and P. G. Bruce, The carbon electrode in nonaqueous Li−O_2 cells, *J. Am. Chem. Soc.*, 2013, **135**, 494–500.

8 D. Cao, Y. Bai, J. Zhang, G. Tan and C. Wu, Irreplaceable carbon boosts Li–O_2 batteries: From mechanism research to practical application, *Nano Energy*, 2021, **89**, 106464.

9 F. Wu, Y. Xing, X. Zeng, Y. Yuan, X. Zhang, R. Shahbazian-Yassar, J. Wen, D. J. Miller, L. Li, R. Chen, J. Lu and K. Amine, Platinum-coated hollow graphene nanocages as cathode used in lithium-oxygen batteries, *Adv. Funct. Mater.*, 2016, **26**, 7626–7633.

10 M. Liu, K. Sun, Q. Zhang, T. Tang, L. Huang, X. Li, X. Zeng, J. Hu and S. Liao, Rationally designed three-dimensional N-doped graphene architecture mounted with Ru nanoclusters as a high-performance air cathode for lithium-oxygen batteries, *ACS Sustain. Chem. Eng.*, 2020, **8**, 6109–6117.

11 T. Fujita, P. Guan, K. McKenna, X. Lang, A. Hirata, L. Zhang, T. Tokunaga, S. Arai, Y. Yamamoto, N. Tanaka, Y. Ishikawa, N. Asao, Y. Yamamoto, J. Erlebacher and M. Chen, Atomic origins of the high catalytic activity of nanoporous gold, *Nat. Mater.*, 2012, **11**, 775–780.

12 J. Lu, Y. J. Lee, X. Luo, K. C. Lau, M. Asadi, H. H. Wang, S. Brombosz, J. Wen, D. Zhai, Z. Chen, D. J. Miller, Y. S. Jeong, J. B. Park, Z. Z. Fang, B. Kumar, A. Salehi-Khojin, Y. K. Sun, L. A. Curtiss and K. Amine, A lithium-oxygen battery based on lithium superoxide, *Nat*, 2016, **529**, 377–382.

13 P. Li, W. Sun, Q. Yu, P. Yang, J. Qiao, Z. Wang, D. Rooney and K. Sun, An effective three-dimensional ordered mesoporous $CuCo_2O_4$ as electrocatalyst for Li–O_2 batteries, *Solid State Ionics*, 2016, **289**, 17–22.

14 G. Liu, L. Zhang, S. Wang, L.-X. Ding and H. Wang, Hierarchical $NiCo_2O_4$ nanosheets on carbon nanofiber films for high energy density and long-life Li–O_2 batteries, *J. Mater. Chem.*, 2017, **A5**, 14530–14536.

15 X. Luo, M. Piernavieja-Hermida, J. Lu, T. Wu, J. Wen, Y. Ren, D. Miller, Z. Z. Fang, Y. Lei and K. Amine, Pd nanoparticles on ZnO-passivated porous carbon by atomic layer deposition: an effective electrochemical catalyst for Li-O_2 battery, *Nanotechnol*, 2015, **26**, 164003.

16 W. Yin, Y. Shen, F. Zou, X. Hu, B. Chi and Y. Huang, Metal−organic framework derived ZnO/$ZnFe_2O_4$/C nanocages as stable cathode material for reversible lithium–oxygen batteries, *ACS Appl. Mater. Interfaces*, 2015, **7**, 4947–4954.

17 L. Dai, X. Zhou, Y. Yang, P. Hu and L. Ci, Ordered porous Mn–Co spinel oxide ($CoMn_2O_4$) with vacancies modulation as efficient electrocatalyst for Li−O_2 battery, *J. Colloid Interface Sci.*, 2024, **670**, 719–728.

18 Y. Lin, J. Bao, S. Zhang, Y. Zhang, J. Qiu, Y. Li, Y. Quan, M. Yuan, G. Sun and C. Nan, Ruthenium highly dispersed in low crystallinity cobalt oxide as an efficient catalyst for Li–O_2 battery, *J. Power Sources*, 2024, **623**, 235394.

19 J. Kim, I. Kang, S. Kim and J. Kang, Facile synthesis of partially oxidized Mn_3O_4-functionalized carbon cathodes for rechargeable Li–O_2 batteries, *RSC Adv.*, 2018, **8**, 22226.

© 2025 The Author(s). Published by the Royal Society of Chemistry

Open Access Article. Published on 11 August 2025. Downloaded on 6/15/2026 7:57:33 AM. This article is licensed under a Creative Commons Attribution 3.0 Unported Licence.

20 J. Kim and J. Kang, An efficient electrocatalyst of NiO supported on carbon paper for nonaqueous Li–O_2 batteries, *Ionics*, 2019, **25**, 5611–5616.
21 I. Kang and J. Kang, Direct growth of CuO particles on carbon papers for high-performance rechargeable Li–O_2 batteries, *J. Nanosci. Nanotechnol.*, 2021, **21**, 3903–3908.
22 I. Kang and J. Kang, Low-cost iron-based electrocatalysts for high-performance Li–O_2 batteries, *Results Mater.*, 2023, **17**, 100351.
23 I. Kang and J. Kang, A novel $CaCO_3$-embedded carbon cathode for highly energy-efficient Li–O_2 batteries, *Ionics*, 2024, **30**, 5189–5195.
24 S. W. Suciyati, J. Junaidi, R. Situmeang and P. Manurung, Nano-ZnO prepared by using chaya and mango leaves extract for photocatalyst of methylene blue, *J. Met., Mater. Miner.*, 2024, **34**, 1848.
25 S. Songpanit, K. Boonyarattanakalin, W. Pecharapa and W. Mekprasart, ZnO nanostructures synthesized by one-step sol-gel process using different zinc precursors, *J. Met., Mater. Miner.*, 2024, **34**, 1968.
26 C. Srikanth and G. M. Madhu, Effect of nano CdO-ZnO content on structural, thermal, optical, mechanical and electrical properties of epoxy composites, *J. Met., Mater. Miner.*, 2023, **33**, 38–52.
27 O. Lupan, T. Pauporté, B. Viana, P. Aschehoug, M. Ahmadi, B. R. Cuenya, Y. Rudzevich, Y. Lin and L. Chow, Eu-doped ZnO nanowire arrays grown by electrodeposition, *Appl. Surf. Sci.*, 2013, **282**, 782–788.
28 O. Lupan, G. A. Emelchenko, V. V. Ursaki, G. Chai, A. N. Redkin, A. N. Gruzintsev, I. M. Tiginyanu, L. Chow, L. K. Ono, B. R. Cuenya, H. Heinrich and E. E. Yakimov, Synthesis and characterization of ZnO nanowires for nanosensor applications, *Mater. Res. Bull.*, 2010, **45**, 1026–1032.
29 J. Liqiang, W. Dejun, W. Baiqi, L. Shudan, X. Baifu, F. Honggang and S. Jiazhong, Effects of noble metal modification on surface oxygen composition, charge separation and photocatalytic activity of ZnO nanoparticles, *J. Mol. Catal. A: Chem.*, 2006, **244**, 193–200.
30 Q. Sun, Z. Guo, T. Shu, Y. Li, K. Li, Y. Zhang, L. Li, J. Ning and K. X. Yao, Lithium-Induced Oxygen Vacancies in MnO_2@MXene for High-Performance Zinc–Air Batteries, *ACS Appl. Mater. Interfaces*, 2024, **16**, 12781–12792.
31 Y.-H. Zhang, S. Zhang, N. Hu, Y. Liu, J. Ma, P. Han, Z. Hu, X. Wang and G. Cui, Oxygen vacancy chemistry in oxide cathodes, *Chem. Soc. Rev.*, 2024, **53**, 3302–3326.
32 Y. Zhang, S. Zhang, J. Ma, A. Huang, M. Yuan, Y. Li, G. Sun, C. Chen and C. Nan, Oxygen Vacancy-Rich RuO_2–Co_3O_4 Nanohybrids as Improved Electrocatalysts for Li–O_2 Batteries, *ACS Appl. Mater. Interfaces*, 2021, **13**, 39239–39247.
33 K. M. Wong, Y. Fang, A. Devaux, L. Wen, J. Huang, L. D. Colac and Y. Lei, Assorted analytical and spectroscopic techniques for the optimization of the defect-related properties in size-controlled ZnO nanowires, *Nanoscale*, 2011, **3**, 4830.
34 R. Hailili, H. Ji, K. Wang, X. Dong, C. Chen, H. Sheng, D. W. Bahnemann and J. Zhao, ZnO with Controllable Oxygen Vacancies for Photocatalytic Nitrogen Oxide Removal, *ACS Catal.*, 2022, **12**, 10004–10017.
35 W. Fan, B. Wang, X. Guo, X. Kong and J. Liu, Nanosize stabilized Li-deficient $Li_{2-x}O_2$ through cathode architecture for high performance Li–O_2 batteries, *Nano Energy*, 2016, **27**, 577–586.
36 E. Yilmaz, C. Yogi, K. Yamanaka, T. Ohta and H. R. Byon, Promoting Formation of Noncrystalline Li_2O_2 in the Li–O_2 Battery with RuO_2 Nanoparticles, *Nano Lett.*, 2013, **13**, 4679–4684.
37 Y. Zhang, X. Li, M. Zhang, S. Liao, P. Dong, J. Xiao, Y. Zhang and X. Zeng, IrO_2 nanoparticles highly dispersed on nitrogen-doped carbon nanotubes as an efficient cathode catalyst for high-performance Li–O_2 batteries, *Ceram. Int.*, 2017, **43**, 14082–14089.
38 G. Yi, G. Li, S. Jiang, G. Zhang, L. Guo, X. Zhang, Z. Zhao, Z. Zou, H. Ma, X. Fu, Y. Liu and F. Dang, Efficient Fe_3C-CF Cathode Catalyst Based on the Formation/Decomposition of $Li_{2-x}O_2$ for Li–O_2 Batteries, *Molecules*, 2023, **28**, 5597.
39 D. Cao, C. Tan and Y. Chen, Oxidative decomposition mechanisms of lithium carbonate on carbon substrates in lithium battery chemistries, *Nat. Commun.*, 2022, **13**, 4908.
40 J. H. Lee, H. W. Jung, I. S. Kim, M. Park and H.-S. Kim, Electrochemical Evaluation of Surface Modified Free-Standing CNT Electrode for Li–O_2 Battery Cathode, *Energies*, 2021, **14**, 4196.

© 2025 The Author(s). Published by the Royal Society of Chemistry